

Combined Spectral and Timing Analysis of the Black Hole Candidate MAXI J1659–152 Discovered by MAXI and Swift

Kazutaka YAMAOKA¹, Ryan ALLURED², Philip KAARET², Jamie A. KENNEA³, Toshihiro KAWAGUCHI⁴, Poshak GANDHI⁵, Nicholai SHAPOSHNIKOV^{6,7}, Yoshihiro UEDA⁸, Satoshi NAKAHIRA⁹, Taro KOTANI¹⁰, Hitoshi NEGORO¹¹, Ichiro TAKAHASHI¹, Atsumasa YOSHIDA¹, Nobuyuki KAWAI¹², and Satoshi SUGITA¹³

¹*Department of Physics and Mathematics, Aoyama Gakuin University, 5-10-1 Fuchinobe, Sagamihara, Chuo-ku, Kanagawa 252-5258, Japan*
yamaoka@phys.aoyama.ac.jp

²*Department of Physics and Astronomy, University of Iowa, Van Allen Hall, Iowa City, IA 52242, USA*

³*Department of Astronomy and Astrophysics, Pennsylvania State University, University Park, PA 16802, USA*

⁴*Center for Computational Sciences, University of Tsukuba, Ten-nodai, 1-1-1 Tsukuba, Ibaraki 305-8577, Japan*

⁵*Institute of Space and Astronautical Science (ISAS), Japan Aerospace Exploration Agency (JAXA), 3-1-1 Yoshino-dai, Chuo-ku, Sagamihara, Kanagawa 252-5210, Japan*

⁶*Department of Astronomy, CRESST/University of Maryland, College Park, MD 20742, USA*

⁷*Goddard Space Flight Center, NASA, Astrophysics Science Division, Greenbelt MD 20771, USA*

⁸*Department of Astronomy, Kyoto University, Oiwake-cho, Sakyo-ku, Kyoto 606-8502, Japan*

⁹*MAXI team, RIKEN, 2-1 Hirosawa, Wako, Saitama 351-0198, Japan*

¹⁰*Research Institute for Science and Engineering, Waseda University, 17 Kikui-cho, Shinjuku-ku, Tokyo 162-0044, Japan*

¹¹*Department of Physics, Nihon University, 1-8-14 Kanda-Surugadai, Chiyoda-ku, Tokyo 101-8308, Japan*

¹²*Department of Physics, Tokyo Institute of Technology, 2-12-1 Ookayama, Meguro-ku, Tokyo 152-8551, Japan*

¹³*EcoTopia Science Institute, Nagoya University, Furo-cho, Chikusa-ku, Nagoya 464-8603, Japan*

(Received ; accepted)

Abstract

We report on X-ray spectral and timing results of the new black hole candidate (BHC) MAXI J1659–152 with the orbital period of 2.41 hours (shortest among BHCs)

in the 2010 outburst from 65 Rossi X-ray Timing Explorer (RXTE) observations and 8 simultaneous Swift and RXTE observations. According to the definitions of the spectral states in Remillard & McClintock (2006), most of the observations have been classified into the intermediate state. All the X-ray broadband spectra can be modeled by a multi-color disk plus a power-law with an exponential cutoff or a multi-color disk plus a Comptonization component. During the initial phase of the outburst, a high energy cutoff was visible at 30–40 keV. The innermost radius of the disk gradually decreased by a factor of more than 3 from the onset of the outburst and reached a constant value of $35 d_{10} \cos i^{-1/2}$ km, where d_{10} is the distance in units of 10 kpc and i is the inclination. The type-C quasi-periodic oscillation (QPO) frequency varied from 1.6 Hz to 7.3 Hz in association with a change of the innermost radius, while the innermost radius remained constant during the type-B QPO detections at 1.6–4.1 Hz. Hence, we suggest that the origin of the type-B QPOs is different from that of type-C QPOs, the latter of which would originate from the disk truncation radius. Assuming the constant innermost radius in the latter phase of the outburst as the innermost stable circular orbit, the black hole mass in MAXI J1659–152 is estimated to be 3.6–8.0 M_\odot for a distance of 5.3–8.6 kpc and an inclination angle of 60–75 degrees.

Key words: accretion, accretion disks — black hole physics — stars: individual (MAXI J1659–152) — X-rays: stars

1. Introduction

Black hole candidates (BHCs) are very important objects for the understanding of accretion and jets in high energy astrophysics (see Remillard & McClintock 2006, McClintock & Remillard 2006, and Belloni 2010 for a review). Most of them are close X-ray binaries consisting of a black hole and a low mass companion (Cyg X-1, LMC X-1 and X-3 are persistent high mass exceptions) characterized by outbursts separated by quiescent periods. During a typical outburst, they go through the hard state (or low/hard state), steep power-law state (SPL; or very high state), intermediate state (IMS), and thermal state (or high/soft state), then the hard state and back to the quiescence, although some other state classifications are present (e.g. soft-intermediate and hard-intermediate state in Belloni 2010).

In the hard state, the X-ray spectrum can be approximately explained by a power-law with an exponential cutoff at 100–200 keV. The power spectrum is characterized by strong variability (20–30 %) with band-limited noise. The hard X-ray emission likely originates from thermal Comptonization in a high temperature corona ($\sim 10^9$ K) of soft photons from the disk. On the other hand, the thermal state spectrum is dominated by a soft component which is considered to be a blackbody from the geometrically thin, optically thick accretion disk ($\sim 10^7$

K). This X-ray spectrum is well fit by the multi-color disk (MCD) model (Mitsuda et al. 1984, Makishima et al. 1986), and also by more accurate accretion disk models (e.g. Li et al. 2005, Davis et al. 2005) which have been developed to take into account relativistic effects. The derived innermost radius from the MCD model typically remains constant at a value which might correspond to the innermost stable circular orbit (ISCO), from which an estimate of the BH mass can be found. Thus derived, black hole mass from X-ray data is found to be consistent with the BH mass estimated from the binary kinematics (Ebisawa et al. 1993, Dotani et al. 1997).

Compared to the two main states, both the SPL and IMS are not well understood. They frequently appear during state transitions between the hard and thermal states. Both disk and power-law components are clearly present in the energy spectra, and the power spectra show strong time variability associated with low-frequency QPOs (LFQPOs), seen at 0.1–10 Hz (Remillard & McClintock 2006). Several types of LFQPOs have been identified and classified into type A, B and C by Remillard et al. (2002) and Casella et al. (2005). Type A and B QPOs are characterized by a relatively low coherence (the coherence parameter $Q \lesssim 3$ for type A and $Q \gtrsim 6$ for type B) and a narrow frequency range of 1–8 Hz associated with a weak red-noise component. Features for the type-C QPOs include a high coherence parameter ($Q \gtrsim 10$), a variable frequency (0.1–10 Hz), and strong broadband noise under the QPO. The study of LFQPOs is essential to our understanding of the spectral state transitions in BHCs, but their origin is still a topic of debate.

A new hard X-ray transient was first discovered as Gamma Ray Burst (GRB) 100925A on September 25, 2010 (MJD 55464) by the Swift Burst Alert Telescope (BAT; Barthelmy et al. 2005) (Mangano et al. 2010). The Gas Slit Camera (GSC; Mihara et al. 2011) on board the Monitor of All-sky X-ray Image (MAXI; Matsuoka et al. 2009) independently detected this X-ray transient and localized it to (RA, Dec)=($16^{\text{h}}59^{\text{m}}10^{\text{s}}$, $-15^{\circ}16'05''$) with a 0.2 degree accuracy (Negoro et al. 2010). The source was designated as MAXI J1659–152. The MAXI/GSC data showed that, unlike normal GRBs, the X-ray flux rapidly increased following the discovery. Rossi X-ray Timing Explorer (RXTE; Bradt, Rothschild, & Swank 1993) follow-up observations revealed the source as a BHC from spectral and timing properties (Kalamkar et al. 2010). Due to the Swift BAT prompt GRB trigger and the source’s location well above the Galactic plane, many multi-wavelength observations including radio (van der Horst et al. 2010), submm bands (den Ugarte Postigo et al. 2010), near-infrared (D’Avanzo et al. 2011), optical (Russel et al. 2010), X-rays and GeV gamma-rays (Lucarelli et al. 2010) have been carried out since the discovery. The XMM-Newton, RXTE, and Swift data revealed the presence of X-ray dips in their light curves with a period of 2.41 hours (Kuulkers et al. 2010, 2011, Belloni, Muñoz-Darias, & Kuulkers 2010, Kennea et al. 2011). The amplitude modulation with this period was also confirmed by the optical data in the VSNET-team report (Kuroda et al. 2010). These results indicate that MAXI J1659–152 has the shortest orbital period among all the black hole

candidates (the second shortest one is 3.2 hours for Swift J1753.5–0127 (Zurita et al. 2008)).

Several X-ray results have already been reported in Kalamkar et al. (2011), Muños-Darias et al. (2011) and Shaposhnikov et al. (2011), and Kennea et al. (2011). We shortly summarize results from these four groups who published spectral and timing results using the same RXTE and Swift data sets. Kalamkar et al. (2011) showed a BHC signature based on the hardness-intensity diagram (Homan & Belloni 2005) and timing properties including the LFQPO classification. At almost the same time, Muños-Darias et al. (2011) reported on detailed timing properties, including time lags for QPOs. These two papers mainly focus on timing properties, although they performed spectral fitting with a simple model, i.e. `wabs*(diskbb+powerlaw)`. Shaposhnikov et al. (2011) performed spectral fits with the bulk-motion Comptonization model (`bmc` in XSPEC; Titarchuk, Mastichiadis & Kylafis 1997), and estimated a BH mass of $20 \pm 3 M_{\odot}$ and a distance of 7.6 ± 1.1 kpc using the spectral-timing correlation scaling technique. Results from Swift/UVOT, XRT and BAT data covering MJD 55464 (Day 0) to 55491 (Day 27) were reported by Kennea et al. (2011). They have detected X-ray dips and Type-C QPOs at 0.15–1.9 Hz, particularly during the initial phase of the outburst, and performed broadband fits with XRT and BAT data.

In this paper, we report on detailed spectral modeling and combined spectral and timing results using 8 (quasi) simultaneous Swift/XRT and RXTE/PCA observations, as well as the same RXTE data sets. In Sections 2 and 3, we describe the RXTE follow-up observations and details of spectral and timing analysis of the data. We also show spectral results from Swift/XRT and RXTE/PCA observations. In Section 4, we discuss how our results compare with those from other BHCs, an estimation of the black hole mass of MAXI J1659–152 from spectral results alone, and the physical origin of the low frequency QPOs. Finally, we will conclude this paper with a summary.

2. Observations and Data Analysis

2.1. RXTE

Following the Swift and MAXI discovery of MAXI J1659–152, we triggered RXTE Target of Opportunity (ToO) observations approved in the AO14 Open-Time program to reveal its nature. Our follow-up observations started on September 28, 2010, and two other programs were triggered after our observations and continued until November 8, 2010, when the source was not observable due to the Sun constraint of the satellite. These series of observations contain 65 pointed observations under the observation IDs 95358, 95108 and 95118. The net deadtime-corrected PCA exposure was 134.6 ksec, with an averaged exposure of about 2.1 ksec per pointed observation.

The RXTE carries three scientific instruments: the Proportional Counter Array (PCA; Jahoda et al. 2006), the High Energy X-ray Timing Experiment (HEXTE; Rothschild et al.

1998), and the All-Sky Monitor (ASM; Levine et al. 1996). The PCA consists of five identical proportional counters (PCU 0–4) which are sensitive in the 2–100 keV range, while the HEXTE is composed of two identical NaI(Tl)/CsI(Na) phoswich scintillators (we distinguish the detectors as Cluster A and B) which are sensitive in the 15–250 keV range. All three instruments are still active and working well in space since the launch in December 1995.

We analyzed the RXTE data using the standard FTOOLS, HEADAS version 6.9, provided by NASA Goddard Space Flight Center (GSFC). For the PCA spectral analysis, we used the Standard 2 mode data, which has 16 sec time resolution and 129 energy channels. The selection criteria were: (1) the offset angle is larger than 0.02 degrees; (2) the elevation from the Earth is larger than 10 degrees; (3) the PCU2 is active; and (4) there are no PCU breakdowns. We accumulated the energy spectra from only the top layer of the PCU2. Dip events seen in RXTE/PCA and Swift/XRT data were not excluded in our analysis. The PCA background was estimated from the model for bright sources, which is publicly available at the PCA analysis web site¹. We performed deadtime corrections (the detector deadtime is typically 2–3 %), and added a 0.5% systematic error to each energy bin. Based on the improvement to the RXTE/PCA calibration², the energy range was limited to 3–50 keV. XSPEC version 12.5 was used for spectral fits. The errors are quoted at statistical 90% error. To check the validity of the current response and our analysis method, we analyzed a Crab observation (ObsID: 95802-01-18-00) with a net exposure of 658 sec, taken on October 22, 2010 during the MAXI J1659–152 outburst. The fit is acceptable ($\chi^2/\text{dof}=62.0/77$), and the Crab spectrum in the 3–50 keV range is explained by a power-law with a photon index of 2.12 ± 0.01 and an observed flux of 2.30×10^{-8} erg cm^{−2} s^{−1} in the 2–10 keV range, which is consistent with the nominal values (Toor & Seward 1974).

For the PCA timing analysis, we used the Event mode data³, which has finer time resolutions than the standard mode data. The power density spectra (PDS) were produced using a light curve binned with a 7.8125 msec time resolution (Nyquist frequency: 64 Hz) and `powspec` in the XRONOS package. The PDS were normalized to a unit of $(\text{rms}/\text{mean})^2$ Hz^{−1} after subtracting the Poisson noise.

Since January 2010, the pointing directions of HEXTE Cluster A and B have been fixed toward the target position and the 1.5°-offset background position. Hence, we needed to use the background production tool `hextebackest`, which predicts the background spectrum for Cluster A from that of Cluster B. However, the HEXTE data were not used because the current version of `hextebackest` still leaves some systematic features at ∼60 keV in the background-subtracted spectra.

¹ http://heasarc.gsfc.nasa.gov/docs/xte/pca_news.html

² Updated on August 26, 2009 at <http://www.universe.nasa.gov/xrays/programs/rxte/pca/doc/rmf/pcarmf-11.7/>

³ The Good Xenon mode and Binned mode data were used during some observations.

2.2. *Swift/XRT*

BHCs have a typical innermost disk black-body temperature of ~ 1 keV (i.e. an emission peak of the blackbody at ~ 2.8 keV) so we only see a Wien tail of the disk blackbody spectrum in the PCA energy range above 3 keV. Hence, there may be large uncertainties in disk parameter estimations of the MCD model, especially when the disk temperature is lower than ~ 0.6 keV. We, therefore, performed fits of MAXI J1659–152 with Swift X-Ray Telescope (XRT; Burrows et al. 2005) data, with soft band coverage over 0.3–10 keV, to obtain reliable disk parameters. In the archived XRT data, we found 7 observations that were exactly simultaneous to RXTE observations, and one (Period H) that was partially simultaneous. The list of simultaneous observations and time intervals is shown in Table 1. All the XRT observations reported in this paper were performed in the Windowed Timing (WT) mode. The XRT data were analyzed in the public web interface⁴ (Evans et al. 2009), and the latest version of the XRT response matrix, swxwt0to2s6_20070901v012.rmf, was used. The energy range was limited to 0.6–9 keV taking into account a calibration uncertainty at low energy and photon statistics at high energy.

3. Results

3.1. *PCA Light Curve and State Classification*

The RXTE/PCA PCU2 light curves with a time resolution of 16 sec in four energy ranges (2–4, 4–10, 10–20, 2–20 keV) are shown in Figure 1. The data were normalized to the PCU2 counts for the Crab nebula. The MAXI/GSC⁵, the RXTE/ASM⁶, the Swift/BAT⁷ data were taken from the web sites for each instrument team, and also normalized to the Crab and are shown for comparison. The flux measurements between PCA and MAXI are consistent with each other. The soft band flux in the 2–10 keV range slowly rises with some variability, while the hard band flux rapidly rises within a few days and then slowly decreases. The approximate e-folding time is about 30 days at high energies. On October 15, 2010, the peak was about 300 mCrab in the 2–20 keV range, and the total outburst duration was about 65 days, assuming the MAXI/GSC and Swift/BAT data cover the whole outburst.

We classified all the observations into accretion states following the definitions in Remillard & McClintock (2006). Note that our classification is based on fitting results with the `wabs*(diskbb+powerlaw)` model in the 3–50 keV range, with a cutoff and iron line during some of the early observations. We found that all the observations were classified into just two states: 58 IMSs and 7 hard states. Neither the thermal state nor the SPL state were observed. The source was initially in the hard state for ~ 4.1 days, then transitioned into the IMS, where

⁴ http://www.swift.ac.uk/user_objects/

⁵ <http://maxi.riken.jp/top>

⁶ <http://heasarc.nasa.gov/docs/xte/ASM/sources.html>

⁷ <http://heasarc.nasa.gov/docs/swift/results/transients/>

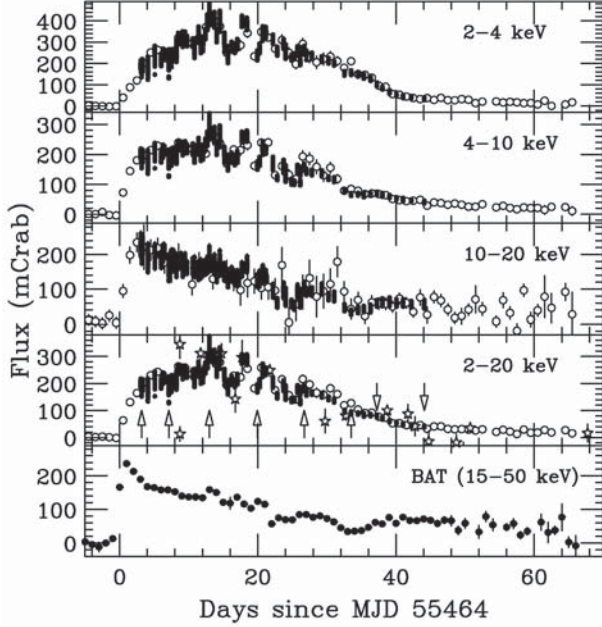


Fig. 1. RXTE/PCA light curves of MAXI J1659–152 during the 2010 outburst. The 2–4, 4–10, 10–20, and 2–20 keV ranges are shown with a 16-sec time bin in the upper four panels. The one-day averaged MAXI/GSC and RXTE/ASM data are superposed on the PCA data with open circles and open stars respectively. The daily averaged Swift/BAT data are also shown in the bottom panel for comparison. The arrows in the 4th panel from the top indicate 8 representative observations for which the spectra and the power spectra are plotted in Figure 2 and 6, respectively.

it remained for 32 days. It finally returned to the hard state around MJD 55503 (day 39). No intense power-law flares as seen in , e.g., XTE J1550–564 (Sobczak et al. 2000) and H 1743–322 (McClintock et al. 2009) were observed.

3.2. Spectral fitting results

3.2.1. RXTE/PCA

We first fit the PCA spectra with a disk blackbody (or MCD model; Mitsuda et al. 1984) plus a power-law modified with the Galactic absorption (i.e. `wabs*(diskbb+powerlaw)`) which are typical components in the X-ray spectra of BHs. However, a reflection-like structure was found above 7 keV. In addition, a high energy cutoff was required at 30–40 keV in some observations during the initial phase of the outburst. Hence we used the model `wabs*(diskbb+smedge*cutofffp)` (hereafter model A) throughout all the data. The hydrogen column density (N_{H}) in `wabs` was fixed at the Galactic value of $1.7 \times 10^{21} \text{ cm}^{-2}$ (Kalberla et al. 2005) following Kalamkar et al. (2011) since the PCA can not determine N_{H} due to the lack of low energy sensitivity. Using a slightly higher value of $3 \times 10^{21} \text{ cm}^{-2}$ (see Section 3.2.2), we found that the fitting results did not change significantly. The energy and the width of the smeared edge (Ebisawa et al. 1994) were fixed at 7.11 keV and 10 keV due to the neutral iron-K edge. The averaged χ^2 is 56.5 for 73 degrees of freedom (d.o.f.) and the maximum χ^2

is 86.5, suggesting that our spectral fits are reasonable. We also tried two other spectral models, `wabs*(diskbb+cutofffp+gaussian)` and `wabs*(diskbb+pexrav)`, using a narrow Gaussian line at 6.4 keV or a reflection component instead of the smeared edge. However, we found that model A gives better fits than these two models (the average χ^2 is 63.3 and 57.9 for 72 d.o.f. for `wabs*(diskbb+cutofffp+gaussian)` and `wabs*(diskbb+pexrav)`, respectively). To show the time variation of spectral and timing parameters over the course of the outburst, we selected 8 observations including 2 hard states and 6 IMSSs as representatives. Figure 2 shows the νF_ν spectra for them.

Time variation of the spectral parameters (innermost `diskbb` temperature T_{in} , innermost radius r_{in} ⁸ (hereafter we assume $D=10$ kpc and $i=0^\circ$ for simplicity when quoting r_{in}), photon index Γ , and e-folding energy E_f), the disk flux, the cutoff power-law (CPL) flux, and the total flux in the 2–20 keV range are shown in Figure 3. Note that the observed T_{in} and r_{in} are not physical because of the spectral hardening due to the electron scattering in the innermost part of the accretion disk and also the lack of the innermost boundary condition in the MCD model (see Section 4.2).

T_{in} increases from ~ 0.5 to a peak of ~ 0.8 keV (day 18), and then drops down to 0.5 keV in the decaying phase. During the initial and final phases, where the source is mainly in the hard state, the r_{in} shows some variations with large error bars. Although the fits require the disk component, the disk estimation might have large uncertainties due to a low sensitivity below 3 keV of RXTE/PCA (see Section 3.2.2). In fact, we directly compare the T_{in} measured by Swift/XRT published in Kennea et al. (2011), and found that the differences were significant during the hard state (0.5–0.6 keV for the PCA versus 0.3–0.4 keV for the XRT). T_{in} never exceeds 1 keV, which has been observed in bright BHCs (e.g. GRO J1655–40 (Sobczak et al. 1999), H 1743–322 (McClintock et al. 2009), and XTE J1550–564 (Sobczak et al. 2000)). In spite of variations of T_{in} and the disk flux, the innermost radius r_{in} remains constant at ~ 30 km.

The Γ of the CPL component smoothly varies from 1.6 to 2.4 and then back to 1.6. During a few observations in the initial phase, a high energy cutoff at 30–40 keV is required in the fits. This is a bit low compared with typical values of 100–200 keV in the hard state (Grove et al. 1998). Some BHCs show a lower cutoff during the initial bright hard state, which is probably due to the rapid increase of the Compton cooling of a high temperature corona by soft disk photons (Miyakawa et al. 2008). The hypothesis that the coronal temperature is controlled by the disk flux will be discussed later (see Figure 8 and §4.1). The flux of the hard CPL component is independent of the disk-flux variation as generally seen in many BHCs.

Steiner et al. (2009a) have pointed out that the hard power-law component diverges at low energies in the `wabs*(diskbb+powerlaw)` model. This situation is unphysical because the

⁸ $r_{\text{in}} = N_{\text{dbb}}^{1/2} (D/10\text{kpc}) \cos i^{-1/2}$, proportional to the square root of N_{dbb} , where N_{dbb} is the normalization of the `diskbb` model, i is the inclination angle (face-on for $i=0^\circ$), and D is the distance to the source.

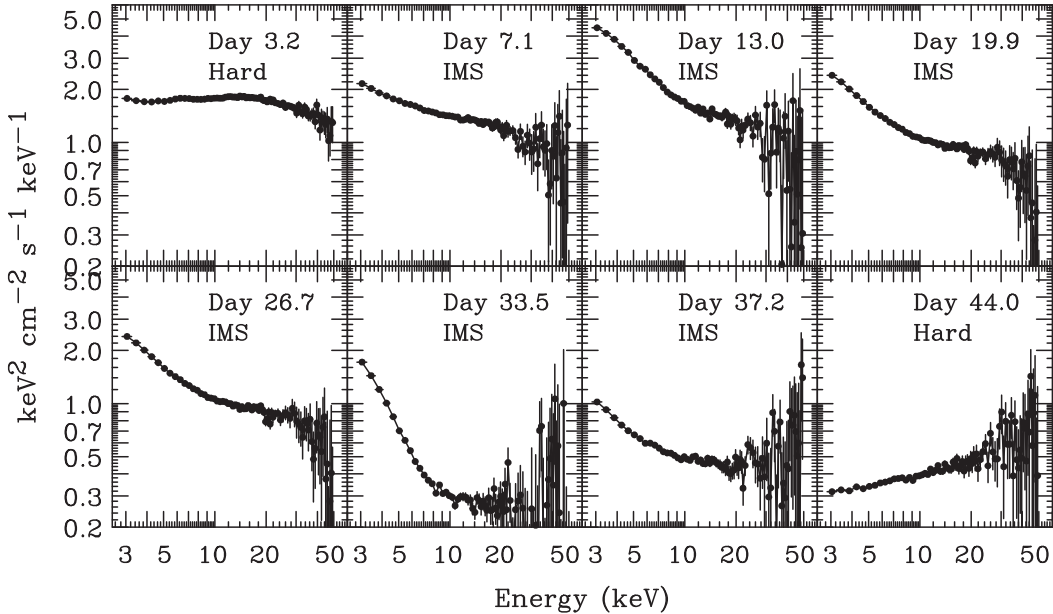


Fig. 2. RXTE/PCA $\nu F\nu$ spectra in the 3–50 keV range for typical observations. The shape of the energy spectra dramatically changed during the outburst. Day indicates days since MJD 55464 (=September 25, 2010).

power-law spectrum results from the Comptonization of disk photons. Hence, they developed a self-consistent Comptonization model, `simpl`, in XSPEC. Because the power-law component of MAXI J1659–152 remained relatively strong throughout the outburst, we used this model as a more accurate estimation for the disk parameters (i.e. `wabs*smedge*highecut*simpl⊗diskbb`, where \otimes means a convolution—hereafter model B). We used the up-scattering only option in `simpl`. The quality of the fitting with this model was almost the same as in model A, yielding an averaged χ^2 of 56.8 for 73 d.o.f. The time variation of the fitting parameters is shown in Figure 4. Model B fits result in larger innermost radii, r_{in} , than those of model A because the `simpl` Comptonization model takes into account the contribution of the disk photons which are scattered into the power-law component as well as direct disk emission. The innermost radius is still roughly constant; there is an initial drop from ~ 50 km to ~ 35 km, where it remains for most of the outburst.

3.2.2. Simultaneous Broadband Fits between Swift/XRT and RXTE/PCA

We fit the Swift/XRT and RXTE/PCA spectra simultaneously using models A and B described in Section 3.2.1. To take into account the calibration uncertainties between the two instruments, the PCA spectra were normalized to the XRT spectra, multiplying the PCA spectra by a constant factor. We found that this normalization factor was reasonably consistent with unity within a 20% accuracy. The hydrogen column density N_{H} was left free.

Figure 5 shows the best-fit broadband spectra for 4 out of 8 simultaneous observation periods. The disk blackbody component becomes more evident later in the outburst. The fits

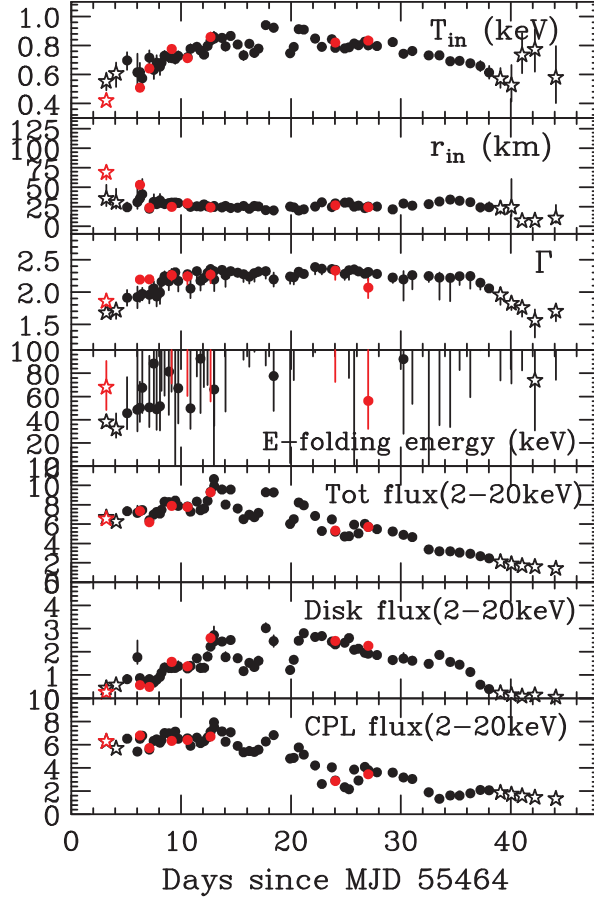


Fig. 3. Time evolution of spectral parameters obtained from model A. The innermost temperature T_{in} , innermost radius r_{in} , photon index Γ , e-folding energy, total flux (2–20 keV), disk flux (2–20 keV), and CPL flux (2–20 keV) are shown from top to bottom. The fluxes are given in units of $10^{-9} \text{ erg cm}^{-2} \text{ s}^{-1}$. The red symbols indicate 8 simultaneous Swift/XRT and RXTE/PCA observations. The hard and intermediate states following definitions in Remillard & McClintock (2006) are shown by open stars and filled circles, respectively.

are reasonable for both models giving reduced chi-squares of 1.0–1.4 for 360 to 500 d.o.f. The best-fit parameters are shown in Table 2. The N_{H} measured in simultaneous fits is almost consistent with the Galactic value $0.17 \times 10^{22} \text{ cm}^{-2}$ for model B, and model A results in a slightly higher value, by $\sim 0.1 \times 10^{22} \text{ cm}^{-2}$, than this value. Their time evolution, shown by red symbols in Figures 3 and 4, displays similar behavior to the results from the RXTE data fits. However, there are significant differences between observations with a lower disk flux than $\sim 1 \times 10^{-9} \text{ erg cm}^{-2} \text{ s}^{-1}$, mainly during the hard states; the fits with RXTE data alone tend to give significantly higher T_{in} and smaller r_{in} than those obtained from the Swift+RXTE fits. Thanks to the joint broadband data, we deduce the reduction of r_{in} (by more than a factor of three from $\sim 110 \text{ km}$ to $\sim 35 \text{ km}$) more precisely than that in the preceding section (from $\sim 50 \text{ km}$ to $\sim 35 \text{ km}$). Hereafter, we do not discuss the disk parameters, T_{in} and r_{in} , obtained from

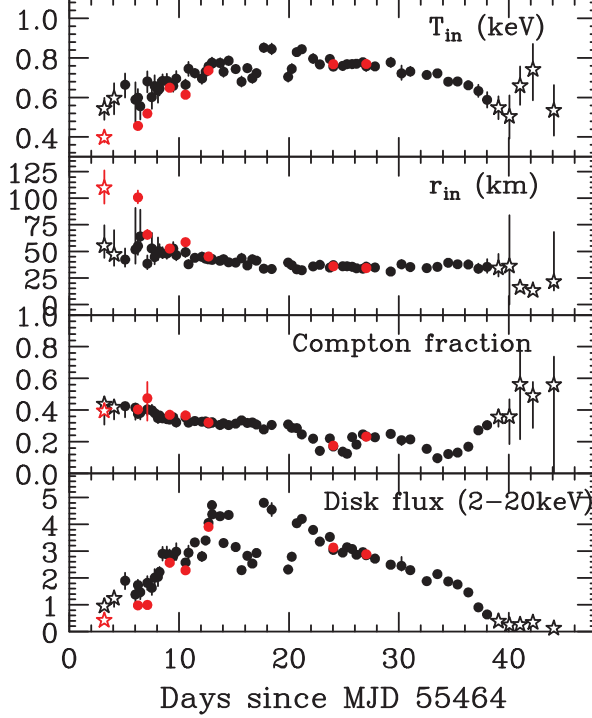


Fig. 4. Time evolution of spectral parameters obtained from model B. The innermost temperature T_{in} , innermost radius r_{in} , Compton fraction, and disk flux in the 2–20 keV range are shown from top to bottom. The symbols and colors are the same as in Figure 3.

RXTE observations alone if the observations had lower disk fluxes than 1×10^{-9} erg cm $^{-2}$ s $^{-1}$ in the 2–20 keV range or were classified in the hard state.

3.3. PCA Timing results

Figure 6 shows the power spectra for 8 representative observations⁹ as displayed by arrows in Figure 1. To derive the QPO characteristics, the power spectra were modeled with a single Lorentzian plus a power-law in a narrow frequency range around the QPO, *i.e.*,

$$P(\nu) = \frac{A^2}{\Delta\nu\pi} \frac{1}{1 + (\frac{\nu - \nu_c}{\Delta\nu})^2} + B\nu^{-\alpha} \quad (1)$$

where ν_c is the QPO central frequency, $\Delta\nu$ is the FWHM width, and A is the QPO amplitude integrated over the full frequency range. The coherence parameter Q is defined by $\nu_c/\Delta\nu$. We focus on the low frequency QPOs (LFQPOs) in these fits because no significant high frequency QPOs were detected. We follow results from Muños-Darias et al. (2011) for the classification of QPOs (Type A, B and C; Casella et al. 2005) between 1 and 8 Hz in 51 of 65 observations; type-B and C were observed in 9 and 42 observations, respectively. The results of central frequency, widths, and the rms variability in the QPO parameters are consistent with Muños-Darias et al. (2011). Figure 7 shows the LFQPO evolution with time. At the beginning

⁹ Please note that these 8 observations are not identical to the 8 simultaneous XRT and PCA observations.

Table 1. List of simultaneous RXTE/PCA and Swift/XRT observations.

Period	Instrument	ObsID	Start Time (UT)	End Time (UT)	State*	QPO†
A (Day 3.2)	RXTE/PCA	95358-01-02-00	2010-09-28 00:54:56	2010-09-28 08:18:56	Hard	C
	Swift/XRT	00434928005	2010-09-28 07:07:02	2010-09-28 07:24:58		
	Time intervals		2010-09-28 07:14:41	2010-09-28 07:24:55		
B (Day 6.3)	RXTE/PCA	95358-01-03-00	2010-10-01 05:46:40	2010-10-01 07:05:04	IMS	C
	Swift/XRT	00434928009	2010-10-01 05:46:02	2010-10-01 06:08:59		
	Time intervals		2010-10-01 05:49:53	2010-10-01 06:08:54		
C (Day 7.1)	RXTE/PCA	95358-01-03-01	2010-10-02 02:32:32	2010-10-02 03:37:36	IMS	C
	Swift/XRT	00434928010	2010-10-02 02:38:02	2010-10-02 03:00:59		
	Time intervals		2010-10-02 02:40:43	2010-10-02 03:00:54		
D (Day 9.1)	RXTE/PCA	95108-01-08-00	2010-10-04 02:43:44	2010-10-04 04:21:52	IMS	C
	Swift/XRT	00434928012	2010-10-04 02:41:02	2010-10-04 03:10:58		
	Time intervals		2010-10-04 02:50:41	2010-10-04 03:10:32		
E (Day 10.6)	RXTE/PCA	95108-01-11-00	2010-10-05 13:46:24	2010-10-05 14:27:44	IMS	C
	Swift/XRT	00434928013	2010-10-05 14:03:02	2010-10-05 14:33:01		
	Time intervals		2010-10-05 14:04:52	2010-10-05 14:14:41		
F (Day 12.7)	RXTE/PCA	95108-01-17-00	2010-10-07 16:01:36	2010-10-07 16:39:44	IMS	C
	Swift/XRT	00434928016	2010-10-07 15:39:02	2010-10-07 16:08:58		
	Time intervals		2010-10-07 16:01:37	2010-10-07 16:08:52		
G (Day 24.0)	RXTE/PCA	95118-01-05-00	2010-10-19 00:25:36	2010-10-19 01:17:52	IMS	no
	Swift/XRT	00031843001	2010-10-19 00:51:02	2010-10-19 01:15:58		
	Time intervals		2010-10-19 01:06:24	2010-10-19 01:15:30		
H (Day 27.0)	RXTE/PCA	95118-01-08-00	2010-10-22 00:38:24	2010-10-22 01:00:00	IMS	no
	Swift/XRT	00031843007	2010-10-22 00:58:02	2010-10-22 01:22:01		
	Time intervals		all intervals for both instruments.			

* Follows definitions in Remillard & McClintock (2006).

† Follows definitions in Casella et al. (2005).

Table 2. Best-fit parameters in simultaneous Swift/XRT and RXTE/PCA observations

Model	Para.	Period A (Day 3.2)		Period B (Day 6.3)		Period C (Day 7.1)		Period D (Day 9.1)	
		model A	model B	model A	model B	model A	model B	model A	model B
wabs	N_{H}^*	$0.27^{+0.01}_{-0.02}$	$0.23^{+0.02}_{-0.02}$	$0.31^{+0.01}_{-0.01}$	$0.23^{+0.01}_{-0.01}$	$0.29^{+0.01}_{-0.01}$	$0.18^{+0.01}_{-0.01}$	$0.34^{+0.02}_{-0.02}$	$0.21^{+0.01}_{-0.01}$
diskbb	$T_{\text{in}}(\text{keV})$	$0.42^{+0.03}_{-0.02}$	$0.40^{+0.03}_{-0.03}$	$0.51^{+0.01}_{-0.01}$	$0.46^{+0.01}_{-0.01}$	$0.64^{+0.02}_{-0.02}$	$0.52^{+0.02}_{-0.02}$	$0.78^{+0.02}_{-0.02}$	$0.65^{+0.01}_{-0.01}$
	$r_{\text{in}}(\text{km})$	$69.0^{+8.9}_{-9.2}$	$109.7^{+16.6}_{-14.9}$	$53.1^{+3.9}_{-3.6}$	$100.8^{+6.3}_{-5.7}$	$23.8^{+2.6}_{-2.4}$	$65.7^{+4.6}_{-4.0}$	$24.7^{+2.3}_{-2.3}$	$52.6^{+2.0}_{-1.9}$
cutofffp/	Γ	$1.86^{+0.05}_{-0.07}$	$1.87^{+0.04}_{-0.06}$	$2.19^{+0.01}_{-0.05}$	$2.22^{+0.01}_{-0.02}$	$2.20^{+0.02}_{-0.05}$	$2.24^{+0.02}_{-0.02}$	$2.26^{+0.07}_{-0.08}$	$2.39^{+0.02}_{-0.02}$
simpl	$E_f(\text{keV})^\dagger$	$68.0^{+22.7}_{-19.7}$	$73.4^{+32.5}_{-20.6}$	>176.3	—	>179.3	—	>61.2	—
	A^\ddagger	$1.46^{+0.07}_{-0.13}$	—	$2.64^{+0.08}_{-0.17}$	—	$2.24^{+0.08}_{-0.15}$	—	$2.88^{+0.29}_{-0.30}$	—
	f^\S	—	$0.39^{+0.02}_{-0.02}$	—	$0.40^{+0.01}_{-0.02}$	—	$0.47^{+0.10}_{-0.14}$	—	$0.37^{+0.01}_{-0.01}$
smedge	τ^{\parallel}	<0.27	<0.21	<0.20	<0.14	<0.27	<0.28	$0.34^{+0.22}_{-0.22}$	$0.47^{+0.15}_{-0.16}$
constant	factor	$1.17^{+0.02}_{-0.02}$	$1.17^{+0.02}_{-0.02}$	$0.94^{+0.01}_{-0.01}$	$0.94^{+0.01}_{-0.01}$	$0.90^{+0.01}_{-0.01}$	$0.89^{+0.01}_{-0.01}$	$0.87^{+0.01}_{-0.01}$	$0.86^{+0.01}_{-0.01}$
$\chi^2/\text{d.o.f.}$		500.1/425	502.2/425	669.4/482	687.8/482	645.6/474	682.7/474	645.6/500	691.2/500
Model	Para.	Period E (Day 10.6)		Period F (Day 12.7)		Period G (Day 24.0)		Period H (Day 27.0)	
		model A	model B	model A	model B	model A	model B	model A	model B
wabs	N_{H}^*	$0.33^{+0.01}_{-0.03}$	$0.21^{+0.01}_{-0.01}$	$0.33^{+0.02}_{-0.03}$	$0.19^{+0.01}_{-0.01}$	$0.30^{+0.01}_{-0.02}$	$0.20^{+0.01}_{-0.01}$	$0.32^{+0.02}_{-0.02}$	$0.24^{+0.01}_{-0.01}$
diskbb	$T_{\text{in}}(\text{keV})$	$0.71^{+0.02}_{-0.02}$	$0.61^{+0.01}_{-0.01}$	$0.86^{+0.03}_{-0.03}$	$0.74^{+0.02}_{-0.02}$	$0.82^{+0.01}_{-0.01}$	$0.77^{+0.01}_{-0.01}$	$0.83^{+0.02}_{-0.01}$	$0.77^{+0.01}_{-0.01}$
	$r_{\text{in}}(\text{km})$	$29.4^{+3.5}_{-3.4}$	$58.7^{+3.2}_{-2.9}$	$24.2^{+2.7}_{-2.3}$	$45.1^{+2.5}_{-2.4}$	$26.7^{+1.3}_{-0.8}$	$35.9^{+1.1}_{-1.1}$	$24.4^{+1.5}_{-1.5}$	$34.3^{+1.1}_{-1.1}$
cutofffp/	Γ	$2.24^{+0.07}_{-0.12}$	$2.35^{+0.03}_{-0.03}$	$2.27^{+0.07}_{-0.13}$	$2.41^{+0.04}_{-0.04}$	$2.33^{+0.03}_{-0.14}$	$2.40^{+0.04}_{-0.04}$	$2.07^{+0.14}_{-0.16}$	$2.35^{+0.04}_{-0.04}$
simpl	$E_f(\text{keV})^\dagger$	>60.3	—	>55.7	—	>72.6	—	$56.2^{+103.4}_{-24.2}$	—
	A^\ddagger	$2.81^{+0.21}_{-0.44}$	—	$3.08^{+0.43}_{-0.49}$	—	$1.42^{+0.11}_{-0.25}$	—	$1.21^{+0.24}_{-0.24}$	—
	f^\S	—	$0.37^{+0.02}_{-0.02}$	—	$0.32^{+0.01}_{-0.01}$	—	$0.17^{+0.01}_{-0.01}$	—	$0.23^{+0.01}_{-0.01}$
smedge	τ^{\parallel}	$0.45^{+0.30}_{-0.29}$	$0.48^{+0.21}_{-0.21}$	$0.60^{+0.36}_{-0.37}$	$0.89^{+0.24}_{-0.24}$	$0.47^{+0.35}_{-0.28}$	$0.81^{+0.25}_{-0.25}$	$0.81^{+0.38}_{-0.38}$	$0.84^{+0.26}_{-0.26}$
constant	factor	$0.97^{+0.02}_{-0.02}$	$0.96^{+0.02}_{-0.02}$	$1.09^{+0.02}_{-0.02}$	$1.09^{+0.02}_{-0.02}$	$0.93^{+0.01}_{-0.01}$	$0.93^{+0.01}_{-0.01}$	$0.87^{+0.01}_{-0.01}$	$0.87^{+0.01}_{-0.01}$
$\chi^2/\text{d.o.f.}$		457.6/409	482.9/409	366.6/363	379.6/363	549.7/462	562.1/462	646.5/495	642.0/495

* In unit of 10^{22} cm^{-2} .

† An e-folding energy in `cutofffp` model or `highcut`.

‡ A normalization of `cutofffp` in unit of photons $\text{cm}^{-2} \text{ s}^{-1}$ at 1 keV.

§ A Compton fraction in `simpl`.

|| An optical depth for the neutral iron K-edge at 7.11 keV.

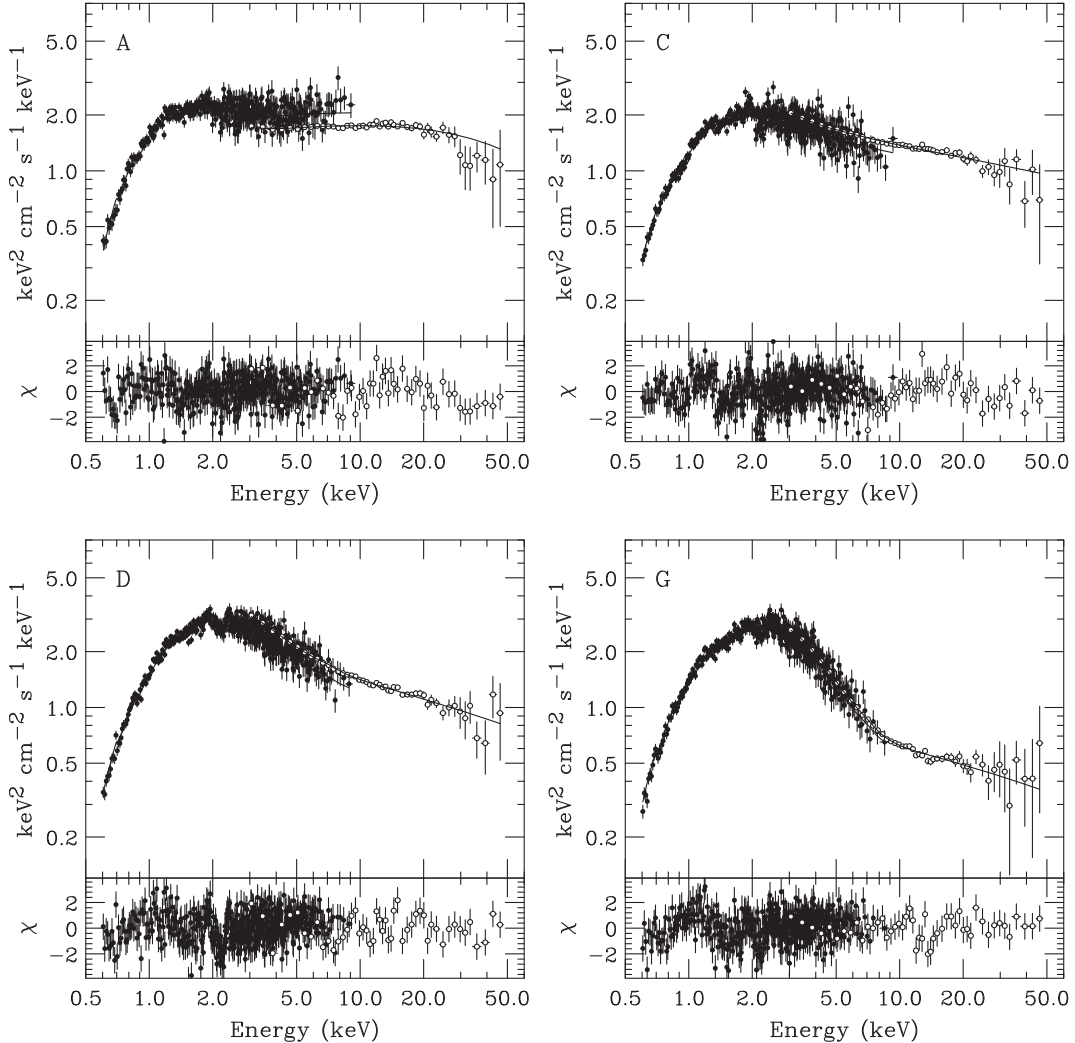


Fig. 5. Spectral fitting results for the Swift/XRT (filled circles) and RXTE/PCA (open circles) data for the period A, C, D, and G (see Table 1). Each upper and lower panel shows the νF_ν spectra with the best-fit model B and residuals from model B respectively.

of the outburst, the frequency of the type-C QPOs gradually increased from 1.6 to 7.3 Hz and then disappeared when the disk fraction was larger than 0.26. Later into the outburst, the type-C QPOs appeared again at 5.9 Hz and decreased down to 1.6 Hz. Type-B QPOs were seen at 1.7–4.1 Hz in the limited time period when the disk fraction was a bit higher than in the case of type-C QPOs. The red noise component under the Type-B QPO is roughly explained by $\nu^{-\alpha}$, where α ranges between 0.7–1.1. This is consistent with ν^{-1} , as typically seen in the thermal state (e.g. McClintock & Remillard 2006).

3.4. Correlation among spectral and timing parameters

To clarify the origin of LFQPOs, we investigated the correlation (or lack thereof) between obtained spectral and timing parameters. Figure 8 shows the correlation of the disk flux in

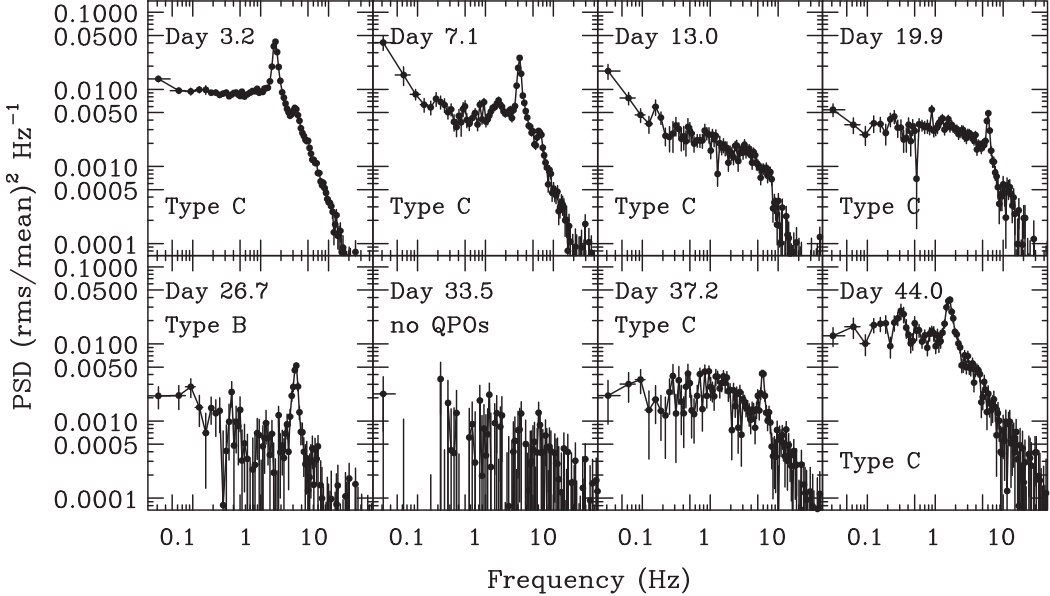


Fig. 6. The power density spectra (PDS) for the 8 representative observations shown in Figure 2. These are produced using the full PCA energy range (2–100 keV). Day means days since MJD 55464 (= September 25, 2010).

the 2–20 keV range with innermost temperature T_{in} , photon index Γ , and Compton fraction. We can see a clear correlation between the disk flux and both T_{in} and Γ , while the Compton fraction is independent of the disk flux. The middle panel (a steeper photon index for a more luminous disk) suggests that the coronal temperature is controlled by the disk flux (see Section 4.1).

Figures 9 and 10 show the QPO frequency ν_c as a function of the disk flux (2–20 keV), T_{in} , r_{in} , Compton fraction, Γ , QPO amplitude A , and rms variability (integrated over 0.1–10 Hz). There is a positive correlation between the type-C QPO ν_c and both the disk flux and T_{in} . We also confirmed the ν_c - Γ correlation already suggested by Shaposhnikov et al. (2011). The correlation is negative with Compton fraction, QPO amplitude A , and fractional rms variability (including the noise component). The slopes of the ν_c - A and ν_c -rms correlations during the type-C QPO detections are almost the same, i.e. $A = -0.017 \pm 0.001 \nu_c(\text{Hz}) + 0.171 \pm 0.005$ and $\text{rms} = -0.019 \pm 0.001 \nu_c(\text{Hz}) + 0.248 \pm 0.002$. The r_{in} obtained from model B shows an anti-correlation with ν_c . This can be explained by $r_{\text{in}}(\text{km}) = 167^{+33}_{-29} \nu_c(\text{Hz})^{-0.70 \pm 0.12}$ for combined XRT and PCA data. All of the correlations obtained by PCA data alone can be confirmed by simultaneous Swift/XRT and RXTE/PCA observations. We also found that the correlation of type-C ν_c does not depend on which state the source was in. This implies that although we have classified the source into two separate states (IMS and hard state), the QPO may have the same physical origin in the different states.

The type-B QPOs show different behavior than the type-C QPOs in the correlation plots.

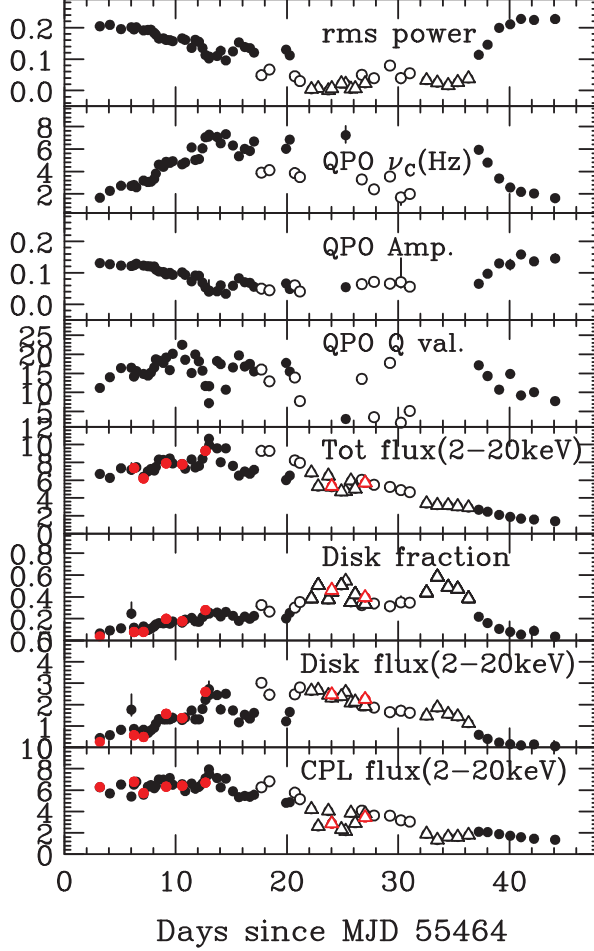


Fig. 7. Time evolution of timing parameters. The rms variability (integrated over 0.1–10 Hz), QPO central frequency ν_c , QPO amplitude A , Q value, total flux (2–20 keV), disk fraction, disk flux (2–20 keV), and CPL flux (2–20 keV) are shown from top to bottom. The open circles, filled circles, and triangles denote observations which showed type-B QPOs, type-C QPOs, and no QPOs, respectively.

There are no correlations of ν_c with r_{in} , Γ , and rms variability. During the type-B QPOs, the innermost radius r_{in} is consistent with a constant value, independent of ν_c , of 33.4 ± 1.2 km (the constant fit gives $\chi^2/\text{dof} = 3.95/8$). This radius could possibly correspond to the ISCO.

4. Discussions

4.1. Short Summary and Comparison with Previous Results and Other Black Hole Binaries

We have presented detailed spectral and timing results from the 2010 outburst of a new BHC, MAXI J1659–152. We used the `simpl` Comptonization model for spectral modeling, and mainly investigated a correlation between spectral parameters and the QPO parameters.

According to the classification criteria given by Remillard & McClintock (2006), the source made a state transition into the intermediate state from the hard state in the early

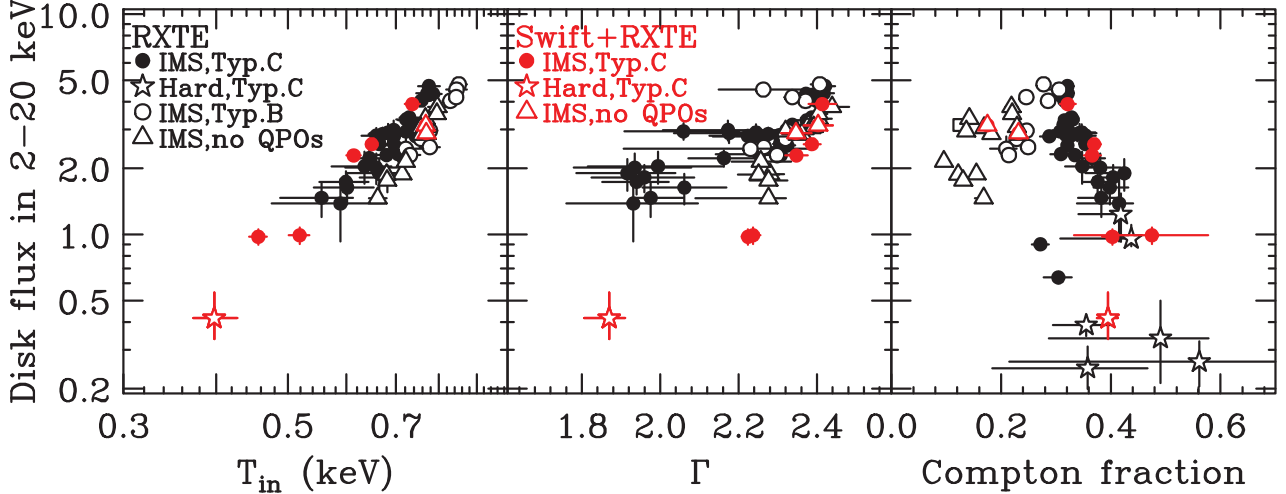


Fig. 8. Correlation between the disk flux in 2–20 keV range and other spectral parameters (innermost temperature T_{in} , photon index Γ , and the Compton fraction.). The results are based on spectral fitting with the model B. The same symbols are used for Figure 7.

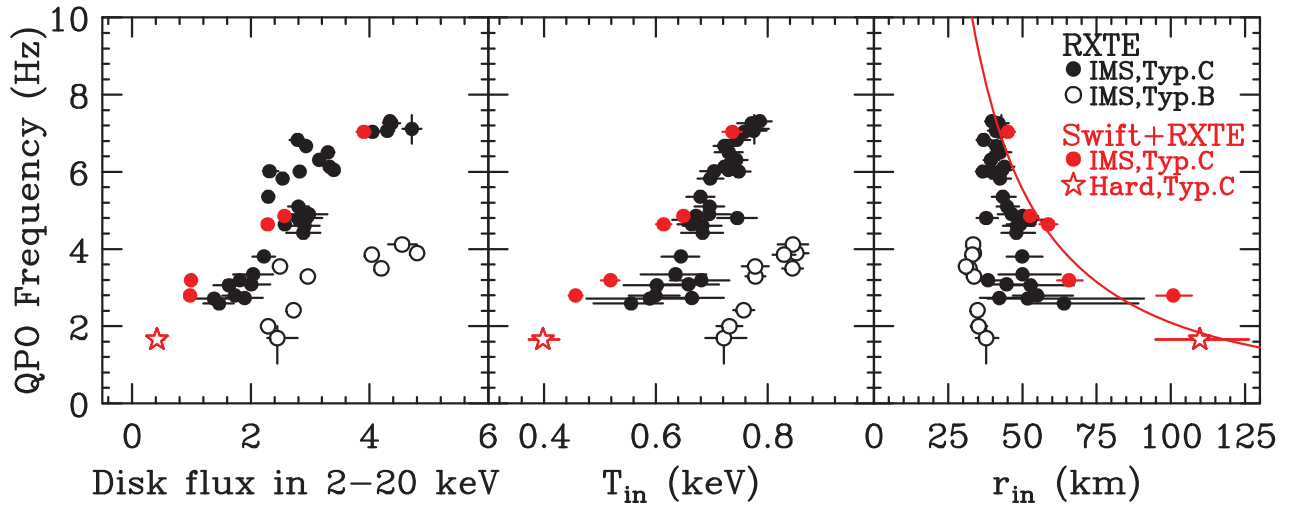


Fig. 9. Correlation between QPO frequency and spectral parameters (disk flux, innermost temperature, and innermost radius) derived from model B. The red line shows the best-fit model ($r_{\text{in}} \propto \nu_c^{-0.70}$) for simultaneous Swift/XRT and RXTE/PCA data. The type-B QPOs, and type-C QPOs during the IMS, and type-C QPOs during the hard state indicates the open circles, filled circles, and open stars, respectively. The red symbol indicates the joint Swift/RXTE observations.

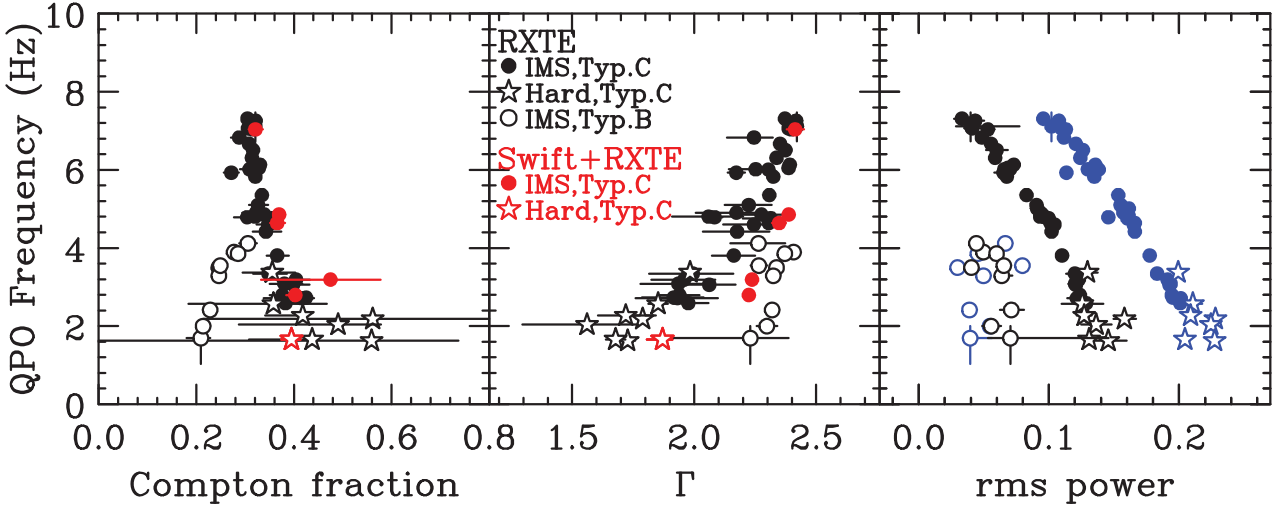


Fig. 10. Correlation between QPO frequency and spectral parameters (II) (Compton fraction and the photon index Γ , the QPO amplitude A (black), and the rms variability integrated over 0.1–10 Hz (blue). The symbols are the same as in Figure 8.

phase and went back to the hard state during the final phase of the outburst. It stayed in the intermediate state during almost of all the observations and never entered into the SPL state or thermal state. This fact is already mentioned by Kalamkar et al. (2011). The RXTE observations revealed that the time evolution of spectral and timing parameters in the 2010 outburst of MAXI J1659–152 are similar to other BHCs (e.g. McClintock & Remillard 2006). The PCA spectra in the 3–50 keV range and XRT+PCA broadband spectra in the 0.6–50 keV range were successfully fit by both the MCD (Mitsuda et al. 1984) plus a power-law with an exponential cutoff and the MCD convolved with `simpl` Comptonization (Steiner et al. 2009a). The maximum T_{in} in the accretion disk was ~ 0.9 keV, which is a bit lower than the typical ~ 1.2 keV seen in bright BHCs such as GRO J1655–40 (Sobczak et al. 1999) and XTE J1550–564 (Sobczak et al. 2000). Since T_{in} is proportional to $\beta^{-1/2}\eta^{1/4}M^{-1/4}$ (Makishima et al. 2000), the Eddington ratio ($\eta=L/L_E$) is relatively low if the BH mass M and spin (related to $\beta=R_{\text{in}}/3R_S$; see Section 4.2) are similar to these bright sources. During the intermediate states, the innermost radius remained almost constant at ~ 30 km (35 km in `simpl` fits) in spite of large variations in the disk flux. The flux variation of the hard CPL component was independent of the disk flux. The photon index in the hard component ranged from 1.6 to 2.4, in correlation with the disk flux, and did not reach typical SPL values of 2.5–3.0 (McClintock & Remillard 2006).

In the initial phase, a high energy cutoff in the power-law component was visible at 30–40 keV. The cutoff energy then evolved into higher energies than the PCA maximum energy (50 keV). The observed e-folding energy is much lower than a typical value in the hard state (100–200 keV; Grove et al. 1998), but a low cutoff energy has been seen for several BHCs during

the rising phase (Miyakawa et al. 2008), probably due to Compton cooling in the corona by soft photons. This could also indicate a transition of the electron distribution from thermal to non-thermal electrons in the corona, but we cannot investigate this issue due to the limited PCA energy range up to 50 keV.

We confirmed results from Kalamkar et al. (2011) and Muños-Darias et al. (2011) that LFQPOs, consisting of type-B and type-C, were observed at 1–8 Hz in 51 of 65 observations. The LFQPOs were seen when both disk and corona components were firmly present, and the disk fraction was less than 35 % (i.e. the hard CPL component was strong). From detailed fits with the `simp1` Comptonization model, we have shown that the type-C QPO central frequency varies from 1.6 Hz to 7.3 Hz in association with the disk flux, the innermost temperature, the innermost radius, the photon index, and the rms variability, similar to that seen in several BHs (e.g. Shaposhnikov & Titarchuk 2009, Vignarca et al. 2003).

Various types of QPOs including low-frequency and high-frequency QPOs have been studied in many X-ray binaries from cataclysmic variables to black holes (Psaltis, Belloni, & van der Klis 1999, Belloni, Psaltis, & van der Klis 2002, Warner, Woudt, & Pretorius 2003), but their origin is still unknown. Several models such as the Lense-Thirring precession model (Stella & Vietri 1998) and the disk oscillation model (Kato 2001) have been proposed. For type-C LFQPOs, we propose a possible scenario based upon the idea of a truncated accretion disk. We assume that the high temperature, corona-like, advection dominated accretion flow (ADAF) is well inside the truncated disk (Esin, McClintock, & Narayan 1997). When the local mass accretion rate from the outer part of the disk increases, the innermost temperature (T_{in}) and the disk flux ($\propto T_{\text{in}}^4$) also increase (see left panel of Figure 8). As the disk flux increases, the corona undergoes cooling due to the Compton scattering of soft photons from the thin disk, and the Compton y parameter ($=\frac{4kT_e}{mc^2} \text{Max}(\tau, \tau^2)$) gets lower (i.e. the photon index gets steeper; see middle panel of Figure 8). The innermost radius of the disk is determined by a balance between the accretion rate and the gas evaporation rate (Meyer, Liu, & Meyer-Hofmeister 2000), and so the innermost radius approaches the ISCO ($3R_S$ (see Section 4.2) corresponding to $r_{\text{in}} \sim 35$ km) from around $9.4R_S$ (~ 110 km) due to a gradual increase of the mass accretion rate.

Shaposhnikov et al. (2011) showed that the type-C QPO rms variability increased with X-ray energy for MAXI J1659–152. Several authors have derived the same results for other BHs (e.g. Casella et al. 2005), naturally implying that the QPO could be of coronal origin. The observed LFQPO frequency (1–8 Hz) is too slow to be explained by the dynamical time scale t_{dyn} (eq.(3.4) in Kato, Fukue, & Mineshige 2008):

$$f_{\text{dyn}} = \frac{1}{t_{\text{dyn}}} = \frac{v_\phi}{2\pi r} = 366 \left(\frac{M}{6M_\odot} \right)^{-1} \left(\frac{r}{3R_S} \right)^{-1.5} \text{Hz} \quad (2)$$

where r is the distance to the BH and v_ϕ is the Keplerian velocity), but can be explained by the viscous time scale t_{vis} (Lynden-Bell & Pringle 1974, eq.(3.71) in Kato, Fukue, & Mineshige 2008):

$$\begin{aligned}
f_{\text{vis}} &= \frac{1}{t_{\text{vis}}} = \alpha \left(\frac{h}{r} \right)^2 f_{\text{dyn}} \\
&= 11.0 \left(\frac{\alpha}{0.03} \right) \left(\frac{h}{r} \right)^2 \left(\frac{M}{6M_{\odot}} \right)^{-1} \left(\frac{r}{3R_{\text{S}}} \right)^{-1.5} \text{Hz},
\end{aligned} \tag{3}$$

where α is the viscous parameter and h is the height of the corona). Here, we adopt α to be 0.03 (Hawley, Gammie, & Balbus 1995, Matsumoto & Tajima 1995, Machida & Matsumoto 2008), the scale height of the corona (h/r) to be 1, and the BH mass to be 6 solar mass (see Section 4.2). Hence, the corresponding frequency to the radius range of 3 to $9.4R_{\text{S}}$, 2.0–11.0 Hz, is in a good agreement with the observed frequency at 1–8 Hz.

If the type-C QPO originates from the neighborhood of the disk truncation radius, we can explain the change of the QPO frequency by a change of the innermost radius. In fact, the observed $r_{\text{in}}-\nu_c$ correlation ($r_{\text{in}} \propto \nu_c^{-0.70 \pm 0.12}$) is remarkably consistent with the above relation $\nu_c \propto r_{\text{in}}^{-1.5}$. A larger innermost radius might result in a larger coronal size, that is, a larger contribution of the hard CPL component, which has more variability than the disk emission in the X-ray spectrum. This could explain the anti-correlation between the QPO frequency and rms variability as seen in right panel of Figure 10.

In contrast, the frequency of type-B QPOs varied from 1.7 to 4.1 Hz, while the innermost radius r_{in} remained constant at ~ 35 km. The constancy of r_{in} suggests that the inner edge of the accretion disk had already reached the ISCO during the type-B QPOs. Thus, a change of the frequency cannot be explained by a change of the disk innermost radius. An innermost-radius independent mechanism (e.g. magnetic reconnection above the thin disk) is necessary for an explanation of type-B QPOs.

The 2010 outburst of MAXI J1659–152 lasted for about two months, a much shorter duration than many other black hole systems (typically more than 100 days; McClintock & Remillard 2006). This short duration is consistent with the fact that MAXI J1659–152 is a small system given its relatively short orbital period (~ 2.41 hours; Kuulkers et al. 2010, 2011). It should be emphasized that all three previously known BHCs with short orbital periods below 6 hours (Swift J1753.5–0127 (3.2 hours; Zurita et al. 2008), XTE J1118+480 (4.1 hours; Uemura et al. 2010), and GRO J0422+32 (5.1 hours; Orosz & Baylin 1995) remained in the hard state during the entire duration of their outbursts. This is probably due to a low mass accretion rate—small accretion disks tend to accumulate less matter than larger disks (Meyer-Hofmeister 2004). As the hardness-intensity diagram seen in Kalamkar et al. (2011) and Muños-Darias et al. (2011) clearly displays a Q-shaped track during the outburst evolution, MAXI J1659–152 might be the first BHC with spectral transitions among the short period BHCs. In addition, all the sources with very short periods are located at high Galactic latitudes ($(l,b)=(5.5, +16.5)$ for MAXI J1659–152, $(157.7, +62.3)$ for XTE J1118+480, $(24.9, +12.2)$ for Swift J1753.5–0127, and $(165.9, -11.9)$ for GRO J0422+32). XTE J1118+480 is thought to be a run-away microquasar which is moving at a high speed of about 100 km s^{-1} (Mirabel et al. 2001), and may

have been born during a supernova on the Galactic disk, and then subsequently moved toward the Galactic halo by kicks received during the explosion. This might suggest that MAXI J1659–152 is also a run-away microquasar similar to XTE J1118+480. The long-term monitoring of radio and/or optical observations of the MAXI J1659–152 source location with high spatial accuracy will be useful for determining the origin of this source. Also, the recently discovered BH transient Swift J1357.2–0933 lies well above the Galactic plane (l,b)=(328.7, +50.0) and stays in the hard state throughout the outburst (Krimm et al. 2011). Swift J1357.2–0933 may thus be a short-period black hole candidate (Torres et al. 2011).

4.2. Estimation of black hole mass

We have evaluated the innermost radius using the `simpl` Comptonization model, and have found that it started at about $110 d_{10} \cos i^{-1/2}$ km, where d_{10} is the distance in units of 10 kpc and i is the inclination angle, during the initial phase and gradually approached the constant value of $\sim 35 d_{10} \cos i^{-1/2}$ km. This could imply that the innermost radius finally reached the ISCO (Ebisawa et al. 1993). Assuming that the ISCO coincides with three times the Schwarzschild radius ($3R_S$), as in the case of a non-spinning Schwarzschild BH, we can estimate the mass of the central object in MAXI J1659–152. However, we note that the observed innermost radius (r_{in}) does not reflect a physical radius (R_{in}) due to two main effects: the MCD model does not assume the torque-free condition at the innermost radius; and the emergent spectrum is distorted by a hardening due to the electron scattering, resulting in a blackbody component with a higher color temperature (T_{col}) than the effective temperature (T_{eff}). We follow the correction method for these two effects that has been developed by Kubota et al. (1998).

Steiner et al. (2009b) applied the `simpl` model to energy spectra taken during intermediate states, and showed that the innermost radius can increase when the Compton fraction is larger than 0.25. So, using the averaged r_{in} value of 35.3 km for $i=0^\circ$ and $D=10$ kpc, weighted for observations with a Compton fraction smaller than 0.25, we can estimate the BH mass as follows:

$$R_{\text{in}} = \xi \kappa^2 r_{\text{in}} = 59.4 \left(\frac{D}{10 \text{kpc}} \right) \left(\frac{\cos i}{\cos 60^\circ} \right)^{-\frac{1}{2}} \text{km} = 82.6 \left(\frac{D}{10 \text{kpc}} \right) \left(\frac{\cos i}{\cos 75^\circ} \right)^{-\frac{1}{2}} \text{km}, \quad (4)$$

where ξ is 0.412 (Kubota et al. 1998) and $\kappa = \frac{T_{\text{col}}}{T_{\text{eff}}}$ is the spectral hardening factor (1.7: Shimura & Takahara 1995). Since we assume R_{in} to be $3R_S$ ($R_S=2GM/c^2$), the obtained black hole mass M is

$$M = \frac{c^2 R_{\text{in}}}{6G} = 6.71 \left(\frac{D}{10 \text{kpc}} \right) \left(\frac{\cos i}{\cos 60^\circ} \right)^{-\frac{1}{2}} M_\odot = 9.32 \left(\frac{D}{10 \text{kpc}} \right) \left(\frac{\cos i}{\cos 75^\circ} \right)^{-\frac{1}{2}} M_\odot. \quad (5)$$

In the case of a rapidly rotating Kerr black hole, the ISCO approaches much closer to the black hole to a minimum of $0.5R_S$, depending on the spin parameter a . In the maximum rotating case ($a \approx 1$), the BH mass estimate can be larger by a maximum factor of 6.

For the mass constraint, we need information for a distance D and an inclination angle i of MAXI J1659–152. We use estimates ($D > 5.3$ kpc and $i = 60\text{--}75^\circ$) suggested by Kuulkers et al. (2011) and Kennea et al. (2011). Furthermore, it is known that the thermal-to-hard transition will occur at 1–4 % of the Eddington luminosity ($L_E = 1.25 \times 10^{38} \frac{M}{M_\odot}$ erg s $^{-1}$) in soft X-ray transients (Maccarone 2003). The observed flux from the hard state after the transition (MJD 55508, day 44.1) was 1.97×10^{-9} erg cm $^{-2}$ s $^{-1}$ in the 3–50 keV range. This was then converted to a bolometric flux of 4.50×10^{-9} erg cm $^{-2}$ s $^{-1}$, assuming a high energy cutoff at 200 keV. Using these three constraints, we plotted the allowed BH mass range by changing the distance and inclination angle in Figure 11. The BH mass is constrained to $3.6\text{--}8.0 M_\odot$ in the 5.3–8.6 kpc range.

For more accurate estimations of disk parameters, we applied the **kerrbb** model (Li et al. 2005) to the RXTE data instead of the **diskbb** model. The **kerrbb** model takes into account relativistic effects (e.g. light bending around the spinning Kerr BH). The spin parameter a was poorly constrained for all the observations, so we fixed a to a value of 0 (i.e. non-spinning BH). The fits using this model were reasonable (average $\chi^2/\text{dof} = 56.1/73$ for $i = 60^\circ$ and $56.2/73$ for $i = 75^\circ$). Assuming $D = 10$ kpc, the BH mass is estimated at $6.7 M_\odot$ for $i = 60^\circ$ and $9.9 M_\odot$ for $i = 75^\circ$, which is in a good agreement with the estimate obtained from the MCD model (equation 5). We also applied the **kerrbb** model to simultaneous Swift and RXTE data in both period G and period H, when the Compton fraction was lower than 0.25. The fitting parameters are shown in Table 3. Assuming $D = 10$ kpc for comparison with the MCD results, the mass is estimated to be $6.18 \pm 0.21 M_\odot$ (period G) and $5.74 \pm 0.21 M_\odot$ (period H) for $i = 60^\circ$, and $9.09 \pm 0.31 M_\odot$ (period G) and $8.46 \pm 0.31 M_\odot$ (period H) for $i = 75^\circ$. The lower limit is $3.27 \pm 0.11 M_\odot$ (period G) and $3.04 \pm 0.11 M_\odot$ (period H) for $i = 60^\circ$ and $D = 5.3$ kpc. These results support the conclusion that the primary object in MAXI J1659–152 is a black hole.

Shaposhnikov et al. (2011) estimated the black hole mass to be $20 \pm 3 M_\odot$ using the empirical correlation among the photon index Γ , the LFQPO frequency, and the normalization in **bmc**. This value is much larger than our estimated one. This discrepancy could be resolved by taking into account the BH spin in our estimation, since the BH mass can increase up to 31–42 M_\odot for the maximum spinning BH ($a \approx 1$) from 5.1–7.1 M_\odot for the non-spinning BH ($a=0$), assuming the estimated distance of 7.6 kpc. Fixing the mass at $20 M_\odot$, the **kerrbb** model fitting for the period G gives $a = 0.91 \pm 0.01$ for $i = 60^\circ$ and $a = 0.84 \pm 0.01$ for $i = 75^\circ$. Dynamic mass measurements using optical observations are expected give more stringent values, and will resolve this issue in the future.

5. Summary

We have presented timing and spectral results from 65 RXTE pointed observations and 8 simultaneous Swift and RXTE observations of the new X-ray transient MAXI J1659–152 in the 2010 outburst. The main results of the study are:

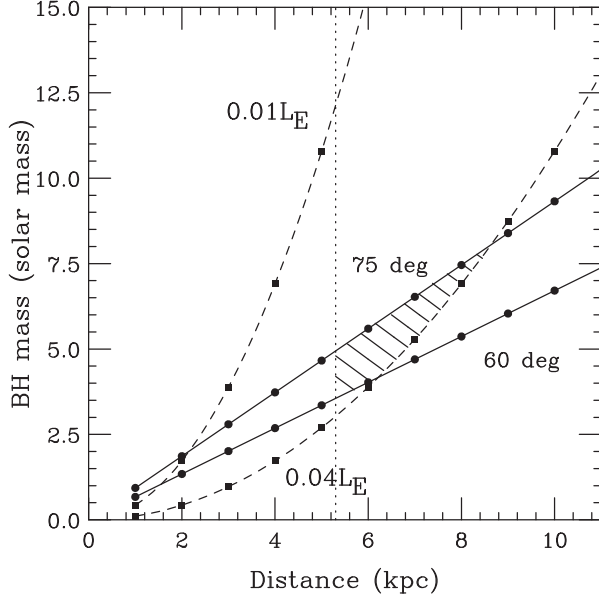


Fig. 11. The allowed range of the black hole mass for MAXI J1659–152, shown by the hatched region. The solid and dashed lines show constraints from the inclination angle of 60–75° and the transition luminosity to the hard state (1–4 % Eddington luminosity), respectively. The dotted line shows a lower limit using the distance 5.3 kpc.

Table 3. Best-fit parameters with **kerrbb** model.

Model	Par.	Period G (Day 24.0)		Period H (Day 27.0)	
		$i=60^\circ$	$i=75^\circ$	$i=60^\circ$	$i=75^\circ$
wabs	N_{H}^*	$0.23^{+0.01}_{-0.01}$	$0.22^{+0.01}_{-0.01}$	$0.27^{+0.01}_{-0.01}$	$0.26^{+0.01}_{-0.01}$
kerrbb [†]	M_{BH}	$6.18^{+0.21}_{-0.21}$	$9.09^{+0.31}_{-0.30}$	$5.74^{+0.21}_{-0.20}$	$8.46^{+0.31}_{-0.30}$
($D=10$ kpc)	\dot{M}^\ddagger	$2.32^{+0.03}_{-0.03}$	$3.81^{+0.06}_{-0.06}$	$2.11^{+0.03}_{-0.03}$	$3.47^{+0.05}_{-0.05}$
kerrbb [†]	M_{BH}	$3.27^{+0.11}_{-0.11}$	$4.82^{+0.17}_{-0.16}$	$3.04^{+0.11}_{-0.11}$	$4.48^{+0.16}_{-0.16}$
($D=5.3$ kpc)	\dot{M}^\ddagger	$0.65^{+0.01}_{-0.01}$	$1.07^{+0.02}_{-0.02}$	$0.59^{+0.01}_{-0.01}$	$0.97^{+0.01}_{-0.01}$
simpl	Γ	$2.34^{+0.04}_{-0.04}$	$2.34^{+0.04}_{-0.04}$	$2.30^{+0.04}_{-0.04}$	$2.30^{+0.04}_{-0.04}$
	f	$0.14^{+0.01}_{-0.01}$	$0.14^{+0.01}_{-0.01}$	$0.20^{+0.01}_{-0.01}$	$0.20^{+0.01}_{-0.01}$
highcut	$E_f(\text{keV})$	—	—	—	—
smedge	τ	$0.20^{+0.27}_{-0.20}$	$0.23^{+0.27}_{-0.23}$	$0.35^{+0.27}_{-0.28}$	$0.37^{+0.27}_{-0.27}$
constant	factor	$0.93^{+0.01}_{-0.01}$	$0.93^{+0.01}_{-0.01}$	$0.87^{+0.01}_{-0.01}$	$0.87^{+0.01}_{-0.01}$
$\chi^2/\text{d.o.f.}$		560.6/462	561.8/462	645.3/495	645.6/495

* In unit of 10^{22} cm $^{-2}$.

[†] Either one of two cases are applied.

[‡] A mass accretion rate in unit of 10^{18} g s $^{-1}$.

1. The outburst lasted about two months, which is shorter than typical outburst duration of BHCs (more than 100 days). Most of the observation epochs are classified into the intermediate state based on definitions in Remillard & McClintock (2006). MAXI J1659–152 might be the first among BHCs with orbital periods shorter than 6 hours to display spectral transitions.
2. X-ray spectral and timing parameters of MAXI J1659–152 are similar to other black hole candidates. The energy spectra in both the 0.6–50 keV and 3–50 keV ranges are well modeled by the MCD model plus a power-law with an exponential cutoff component modified with the smeared edge and Galactic absorption. Both type-B and type-C QPOs were found in the power spectra among 51 observations, when both the disk and corona components are securely present.
3. The maximum innermost temperature was \sim 0.9 keV. This is low compared to typical values of T_{in} observed in bright BHCs (1.0–1.3 keV). The high energy cutoff was present at 30–40 keV during the initial phase of the outburst. This may be due to the Compton cooling of the corona by soft photons at the beginning of the outburst.
4. The central frequency for the type-C QPOs, seen in the range of 1.6–7.3 Hz, is correlated with the innermost temperature, disk flux, and photon index, and is anti-correlated with rms variability and innermost radius. This can be explained by the scenario that the type-C QPO originates from the truncated disk radius. The type-B QPO frequency varied from 1.7 to 4.1 Hz while the innermost radius remained constant at 35 km. Hence, the origin of the type-B QPO is definitely different from that of the type-C QPO.
5. Using combined Swift and RXTE data, we found that the innermost radius decreased by a factor of more than 3 and approached a constant value of 35 km for assumed distance of 10 kpc and inclination of 0 degree during the middle of the outburst. Assuming this constant value to be the ISCO and the black hole to be non-spinning, the black hole mass of MAXI J1659–152 is estimated at 3.6–8.0 M_{\odot} , for a distance of 5.3–8.6 kpc and an inclination angle of 60–75° (Kuulkers et al. 2011, Kennea et al. 2011).

We thank the anonymous referee for his/her useful comments and discussions. This research has made use of: MAXI data provided by RIKEN, JAXA and the MAXI team; Swift/BAT transient monitor results provided by the Swift/BAT team; RXTE/ASM data provided by the ASM/RXTE teams at MIT and at the RXTE SOF and GOF at NASA/GSFC; RXTE/PCA data obtained from the High Energy Astrophysics Science Archive Research Center (HEASARC) provided by NASA/GSFC; and Swift/XRT data supplied by the UK Swift Science Data Centre at the University of Leicester.

References

Barthelmy, S. D. et al. 2005, Space Science Reviews, 120, 143

- Belloni, T., Psaltis, D., & van der Klis, M. 2002, ApJ, 572, 392
- Belloni, T. M., Muñoz-Darias, T., & Kuulkers, E. 2010, Astronomers' Telegram #2926
- Belloni, T. M. 2010, In; T., Belloni(ed.) Lecure Notes in Physics, Berlin Springer Verlag, vol.794, 53
- Bradt, H. V., Rothschild, R. E. & Swank, J. H. 1993, A&AS, 97, 355
- Burrows, D. N., et al. 2005, Space Sci. Rev., 120, 165
- Casella, P., Belloni, T., Homan, J., Stella, L. 2005, ApJ, 629, 403
- D'Avanzo, P., Goldoni, P., Patruno, A., Casella, P., Campana, S., Russell, D. M., & Belloni, T. M. 2011, Astronomers' Telegram #2900
- Davis, S. W., Blaes, O. M., Hubeny, I., Turner, N. J. 2005, ApJ, 621, 372
- den Ugarte Postigo, A., Lundgren, A., Wracks, F., Thoene, C. C., Castro-Tirado, A. J., Gorosabel, J., Jelinek, M. 2010, GCN circ. 11304
- Dotani, T., et al. 1997, ApJ, 485, 87
- Ebisawa, K., Makino, F., Mitsuda, K., Belloni, T., Cowley, A. P., Schmidtke, P. C., Treves, A. 1993, ApJ, 403, 684
- Ebisawa, K., et al. 1994, PASJ, 46, 375
- Esin, A. A., McClintock, J. E., & Narayan, R. 1997, ApJ, 489, 865
- Evans, P. A., et al. 2009, MNRAS, 397, 1177
- Grove, J. E., Johnson, W. N., Kroeger, R. A., McNaron-Brown, K., Skibo, J. G., Philips, B. F. 1998, ApJ, 500, 899
- Homan, J., & Belloni, T. 2005, Ap&SS, 300, 107
- Hawley, J. F., Gammie, C. F., & Balbus, S. A. 1995, ApJ, 440, 742
- Jahoda, K., Markwardt, C. B., Radeva, Y., Rotz, A. H., Stark, M. J., Swank, J. H., Strohmayer, T. E., Zhang, W. 2006, ApJS, 163, 401
- Kalberla, P. M. W., et al. 2005, A&A, 440, 775
- Kalamkar, M., et al. 2010, Astronomers' Telegram #2881
- Kalamkar, M., Homan, J., Altamirano, D., Van Der Klis, M., Casella, P., Linares, M. 2011, ApJ, 731, L2
- Kato, S. 2001, PASJ, 53, 1
- Kato, S., Fukue, J., & Mineshige, S. 2008, Black-Hole Accretion Disks – Towards a New Paragraph —, Kyoto University Press
- Kennea J. A., et al. 2011, ApJ, 736, 22
- Krimm, H. A., et al. 2011, Astronomers' Telegram #3138
- Kubota, A., Tanaka, Y., Makishima, K., Ueda, Y., Dotani, T., Inoue, H., & Yamaoka, K. 1998, PASJ, 50, 667
- Kuroda, D., et al. 2011, proceedings of the 4th international MAXI workshop.
- Kuulkers, E., et al. 2010, Astronomers' Telegram #2912
- Kuulkers, E., et al. 2011, proceedings of the 4th international MAXI workshop, arXiv.1102.2102v1
- Levine, A., Bradt, H., Cui, W., Jernigan, K. G., Morgan, E. H., Remillard, R., Shirey, R. E., Smith, D. A. 1996, ApJ, 469, L33
- Li, L., Zimmerman, E. R., Narayan, R., McClintock, J. E. 2005, ApJS, 157, 335
- Lucarelli, F., et al. 2010, Astronomers' Telegram #2880

- Lynden-Bell, D., & Pringle, J. E. 1974, MNRAS, 168, 603
- Maccarone, T. J. 2003, A&A, 409, 697
- Makishima, K. et al., 1986, PASJ, 36, 741
- Makishima, K. et al., 2000, ApJ, 535, 632
- Mangano, V., Hoversten, E. A., Markwardt, C. B., Sbarufatti, B., Starling R. L. C., Ukwatta, T. N. 2010, GCN circ. 11296
- Matsumoto, R., & Tajima, T. 1995, ApJ, 445, 767
- Machida, M., & Matsumoto, R. 2008, PASJ, 60, 613
- Matsuoka, M., et al. 2009, PASJ, 61, 999
- McClintock, J. E., & Remillard, R. E. 2006, in Lewin, W. & van der Klis, M., eds. Compact Stellar X-ray Sources, Cambridge University Press, Cambridge, ch. 4
- McClintock, J. E., Remillard, R. E., Rupen, M. P., Torres, M. A. P., Steeghs, D., Levine, A. M., Orosz, J. A. 2009, ApJ, 698, 1398
- Meyer, E., Liu, B. F., & Meyer-Hofmeister, E. 2000, A&A, 354, L67
- Meyer-Hofmeister, E. 2004, A&A, 423, 321
- Mihara, T., et al. 2011, PASJ, accepted
- Mirabel, I. F., Dhawan, V., Mignani, R. P., Rodrigues, I., Guglielmetti, F. 2001, Nature, 413, 139
- Mitsuda, K., et al. 1984, PASJ, 36, 741
- Miyakawa, T., Yamaoka, K., Homan, J., Saito, K., Dotani, t., Yoshida, A., Inoue, H. 2008, PASJ, 60, 637
- Muños-Darias, T., Motta, S., Siele, H., Belloni. T. M. 2011, MNRAS, 415, 292
- Negoro, H., et al. 2010, Astronomers' Telegram #2873
- Orosz, J. A., & Baylin, C. D. 1995, ApJ, 446, L59
- Psaltis, D., Belloni, T., & van der Klis, M. 1999, ApJ, 520, 262
- Remillard, R. A., Sobczak, G. J., Munoz, M. P., McClintock, J. E. 2002, ApJ, 564, 962
- Remillard, R. E. & McClintock, J. E. 2006, ARA&A, 44, 49
- Rothschild, R. E., et al. 1998, ApJ, 496, 538
- Russel, D. M., et al. 2010, Astronomers' Telegram #2884
- Shaposhnikov, N., & Titarchuk, L. ApJ, 699, 453
- Shaposhnikov, N., Swank, J. H., Markwardt, C., & Krimm, H. 2011, submitted for the 4th MAXI Workshop Proceedings, arXiv.1103.0531
- Shimura, T., & Takahara, F. 1995, ApJ, 445, 780
- Sobczak, G. J., McClintock, J. E., Remillard, R. A., Bailyn, C. D., Orosz, J. A. 1999, ApJ, 520, 776
- Sobczak, G. J., McClintock, J. E., Remillard, R. A., Cui, W., Levine, A. M., Morgan, E. H., Orosz, J. A., Baylin, C. D. 2000, ApJ, 544, 993
- Steiner, J. F., Narayan, R., McClintock, J. E., Ebisawa, K. 2009a, PASP, 121, 885
- Steiner, J. F., McClintock, J. E., Remillard, R. A., Narayan, R., Gou, L. 2009b, ApJ, 701, L83
- Stella, L., & Vietri, M. 1998, ApJ, 492, L59
- Titarchuk, L., Mastichiadis, A., Kylafis, N. D. 1997, ApJ, 487, 834
- Toor, A., & Seward, F. D. 1974, AJ, 79, 995
- Torres, M. A. P., Steeghs, D., Jonker, P. G., Rauch, M. 2011, Astronomers' Telegram #3143

- Uemura, M., et al. 2000, PASJ, 52, L15
- van der Horst, A. J., Granot, J., Paragi, Z., Kouveliotou, C., Wijers, R. A. M. J., Ramirez-Ruiz, E. 2010, Astronomers' Telegram #2874
- Vignarca, F., Migliari, S., Belloni, T., Psaltis, D., van der Klis, M. 2003, A&A, 397, 729
- Warner, B., Woudt, P. A., & Pretorius, M. L. 2003, MNRAS, 344, 1193
- Zurita, C., Durant, M., Torres, M. A. P., Shahbaz, T., Casares, J., Steeghs, D. 2008, ApJ, 681, 1458